

Air Force Institute of Technology

AFIT Scholar

Faculty Publications

12-3-2012

Bidirectional Scatter Measurements of a Guided-mode Resonant Filter Photonic Crystal Structure

Michael A. Marciniak

Air Force Institute of Technology

Spencer R. Sellers

R. B. Lamott

Air Force Research Laboratory

B. T. Cunningham

University of Illinois at Urbana-Champaign

Follow this and additional works at: <https://scholar.afit.edu/facpub>



Part of the [Electromagnetics and Photonics Commons](#)

Recommended Citation

Marciniak, M. A., Sellers, S. R., Lamott, R. B., & Cunningham, B. T. (2012). Bidirectional scatter measurements of a guided-mode resonant filter photonic crystal structure. *Optics Express*, 20(25), 27242–27252. <https://doi.org/10.1364/OE.20.25.027242>

This Article is brought to you for free and open access by AFIT Scholar. It has been accepted for inclusion in Faculty Publications by an authorized administrator of AFIT Scholar. For more information, please contact richard.mansfield@afit.edu.

Bidirectional scatter measurements of a guided-mode resonant filter photonic crystal structure

M. A. Marciniak,^{1,*} S. R. Sellers,² R. B. Lamott,³ and B. T. Cunningham⁴

¹Department of Engineering Physics, Air Force Institute of Technology, Wright-Patterson AFB Ohio 45433, USA

²Department of Electrical and Computer Engineering, Air Force Institute of Technology, Wright-Patterson AFB Ohio 45433, USA

³Munitions Directorate, Air Force Research Laboratory, Eglin AFB Florida 32542, USA

⁴Department of Electrical and Computer Engineering, University of Illinois at Urbana-Champaign, Urbana, Illinois 61801, USA

*michael.marciniak@afit.edu

Abstract: This work investigates the Bidirectional Scatter Distribution Function (BSDF) at incident angles other than normal and at 544-nm wavelength of a Guided Mode Resonance Filter (GMRF) Photonic Crystal (PC) structure designed for normally incident light at 532 nm. Strong out-coupling of PC diffraction orders into both the transmitted and reflected hemispheres was observed specifically at a 25.7° incidence angle, which we attribute to this incident angle/wavelength pair being a good match to the ($\pm 1, 0$) PC grating mode. BSDF measurements at incident angles of 15° and 35° also displayed some out-coupled diffraction, though much lower in magnitude, and are also attributed to being a weaker match to the ($\pm 1, 0$) PC grating mode. Three-dimensional finite-difference time-domain Maxwell's equation simulations demonstrate that since this GMRF was designed for complete destructive interference of the transmitted light upon normal incidence, stronger out-coupling of the diffraction is expected for modal solutions as the angle of incidence increases.

©2012 Optical Society of America

OCIS codes: (290.1483) BSDF, BRDF, and BTDF; (120.5820) Scattering measurements; (050.5298) Photonic crystals; (050.1755) Computational electromagnetic methods.

References and links

1. N. Fabre, L. Lalouat, B. Cluzel, X. Mélique, D. Lippens, F. de Fornel, and O. Vanbésien, "Optical near-field microscopy of light focusing through a photonic crystal flat lens," *Phys. Rev. Lett.* **101**(7), 073901 (2008).
2. S. N. Tandon, M. Soljacic, G. S. Petrich, J. D. Joannopoulos, and L. A. Kolodziejski, "The superprism effect using large area 2D-periodic photonic crystal slabs," *Photon. Nano. Fund. Appl.* **3**(1), 10–18 (2005).
3. H. Kosaka, T. Kawashima, A. Tomita, M. Notomi, T. Tamamura, T. Sato, and S. Kawakami, "Self-collimating phenomena in photonic crystals," *Appl. Phys. Lett.* **74**(9), 1212–1214 (1999).
4. H. Kurt, E. Colak, O. Cakmak, H. Caglayan, and E. Ozbay, "The focusing effect of graded index photonic crystals," *Appl. Phys. Lett.* **93**(17), 171108 (2008).
5. I. Prieto, B. Galiana, P. A. Postigo, C. Algora, L. J. Martínez, and I. Rey-Stolle, "Enhanced quantum efficiency of Ge solar cells by a two-dimensional photonic crystal nanostructured surface," *Appl. Phys. Lett.* **94**(19), 191102 (2009).
6. T. R. Nielsen, A. Lavrinenko, and J. Mork, "Slow light in quantum dot photonic crystal waveguides," *Appl. Phys. Lett.* **94**(11), 113111 (2009).
7. M. Galli, S. L. Portalupi, M. Belotti, L. C. Andreani, L. O'Faolain, and T. F. Krauss, "Light scattering and Fano resonances in high-*Q* photonic crystal nanocavities," *Appl. Phys. Lett.* **94**(7), 071101 (2009).
8. S. S. Wang and R. Magnusson, "Theory and applications of guided-mode resonance filters," *Appl. Opt.* **32**(14), 2606–2613 (1993).
9. N. Ganesh and B. T. Cunningham, "Photonic-crystal near-ultraviolet reflectance filters fabricated by nanoreplica molding," *Appl. Phys. Lett.* **88**(7), 071110 (2006).
10. F. Yang, G. Yen, and B. T. Cunningham, "Integrated 2D photonic crystal stack filter fabricated using nanoreplica molding," *Opt. Express* **18**(11), 11846–11858 (2010).
11. T. Sun and D. Wu, "Guided-mode resonance excitation on multimode planar periodic waveguide," *J. Appl. Phys.* **108**(6), 063106 (2010).

12. A. Hessel and A. A. Oliner, "A new theory of Wood's anomalies on optical gratings," *Appl. Opt.* **4**(10), 1275–1299 (1965).
13. P. C. Mathias, N. Ganesh, L. L. Chan, and B. T. Cunningham, "Combined enhanced fluorescence and label-free biomolecular detection with a photonic crystal surface," *Appl. Opt.* **46**(12), 2351–2360 (2007).
14. I. Abdulhalim, M. Auslender, and S. Hava, "Resonant and scatterometric grating-based nanophotonic structures for biosensing," *J. Nanophotonics* **1**(1), 011680 (2007).
15. F. Yang, G. Yen, G. Rasigade, J. A. N. T. Soares, and B. T. Cunningham, "Optically tuned resonant optical reflectance filter," *Appl. Phys. Lett.* **92**(9), 091115 (2008).
16. I. Abdulhalim, "Anisotropic layers in waveguides for mode tuning and tunable filtering," *Proc. SPIE* **6135**, 61350R, 61350R-10 (2006).
17. F. Yang, G. Yen, and B. T. Cunningham, "Voltage-tuned resonant reflectance optical filter for visible wavelengths fabricated by nanoreplica molding," *Appl. Phys. Lett.* **90**(26), 261109 (2007).
18. D. W. Dobbs and B. T. Cunningham, "Optically tunable guided-mode resonance filter," *Appl. Opt.* **45**(28), 7286–7293 (2006).
19. I. Abdulhalim, "Simplified optical scatterometry for periodic nanoarrays in the near-quasi-static limit," *Appl. Opt.* **46**(12), 2219–2228 (2007).
20. S.-T. Wu, M. S. Li, and A. Y.-G. Fuh, "Observation of conical scattering cones from a two-dimensional hexagonal photonic crystal based on a polymer-dispersed liquid crystal," *Opt. Lett.* **33**(23), 2758–2760 (2008).
21. J. Boulengueza, S. Berthiera, and J. P. Vigneron, "Simulations tools for natural photonic structures," *Physica B* **394**(2), 217–220 (2007).
22. D. G. Stavenga, H. L. Leertouwer, P. Piri, and M. F. Wehling, "Imaging scatterometry of butterfly wing scales," *Opt. Express* **17**(1), 193–202 (2009).
23. E. Van Hooijdonk, C. Barthou, J. P. Vigneron, and S. Berthier, "Detailed experimental analysis of the structural fluorescence in the butterfly *Morpho sulkowskyi* (Nymphalidae)," *J. Nanophotonics* **5**(1), 053525 (2011).
24. R. V. Nair and R. Vijaya, "Observation of higher-order diffraction features in self-assembled photonic crystals," *Phys. Rev. A* **76**(5), 053805 (2007).
25. J. Allgair, D. Benoit, R. Hershey, L. C. Litt, I. Abdulhalim, B. Braymer, M. Faeyrman, J. C. Robinson, U. Whitney, Y. Xu, P. Zalicki, and J. Seligson, "Manufacturing considerations for implementation of scatterometry for process monitoring," *Proc. SPIE* **3998**, 125–134 (2000).
26. I. Kallioniemi, J. Saarinen, and E. Oja, "Optical scatterometry of subwavelength diffraction gratings: neural-network approach," *Appl. Opt.* **37**(25), 5830–5835 (1998).
27. C. J. Raymond, M. R. Murnane, S. Sohail, H. Naqvi, and J. R. McNeil, "Metrology of subwavelength photoresist gratings using optical scatterometry," *J. Vac. Sci. Technol. B* **13**(4), 1484–1495 (1995).
28. B. L. Balling, "A comparative study of the bidirectional reflectance distribution function of several surfaces as a mid-wave infrared diffuse reflectance standard," MSEE thesis, Air Force Institute of Technology, 2009.
29. T. A. Germer and C. C. Asmail, "Goniometric optical scatter instrument for out-of-plane," *Rev. Sci. Instrum.* **70**(9), 3688–3695 (1999).

1. Introduction

Photonic crystals (PC's) are periodic optical nanostructures that are designed to manipulate the flow of light. Distinct optical phenomena associated with PC structures include negative refraction [1], super-prism [2], self-collimation [3] and lensing [4], light trapping [5] and slow light [6], and Fano resonance [7]. Guided mode resonance filters (GMRF's) are structures in which a one- or two-dimensional (1- or 2-D) PC is embedded in a planar dielectric structure such that a portion of light incident at a particular angle and wavelength is diffracted into that structure where it resonates. The trapped light is then re-diffracted out of the structure such that it interferes destructively with the otherwise transmitted portion of the beam. At the design angle and wavelength, there can be complete interference and no light transmission [8–11]. GMRF structures have been discussed in terms of Wood's anomaly [12], used for biosensing [13,14], and made tunable optically [15] or with liquid crystals [16,17] and dyes [18]. This work investigates the Bidirectional Scatter Distribution Function (BSDF) of a GMRF at incidence angles and wavelengths other than those for which the structure was designed.

The BSDF is the combination of the BRDF (reflectance) and BTDF (transmittance), and is defined as the scattered radiance, L_s , ($\text{W}\cdot\text{cm}^{-1}\cdot\text{Sr}^{-1}$) per incident irradiance, E_i ($\text{W}\cdot\text{cm}^{-2}$). Practically, since the illuminated area in a BSDF experiment is also the (reflected or transmitted) radiant area, the BSDF can be defined as the collected radiant flux, Φ_s , per solid angle, Ω_s (as defined by the detection aperture and its distance from the sample), per incident flux, Φ_i , adjusted for the projected area of the source as viewed by the detector ($\cos \theta_s$):

$$BSDF(\theta_i, \phi_i, \theta_s, \phi_s) = \frac{L_s(\theta_s, \phi_s)}{E_i(\theta_i, \phi_i)} = \frac{\Phi_s / \Omega_s}{\Phi_i(\theta_i, \phi_i) \cos \theta_s} \left(\frac{1}{Sr} \right) \quad (1)$$

BSDF measurement of PC's in the literature is sparse, including periodic nanoarrays [19], 2-D hexagonal PC's [20], natural PC's [21–23], self-assembled PC's [24], and even including critical dimension metrology [25–27]. This work presents novel BSDF and spectral collinear transmittance measurements of a GMRF PC structure, along with supporting analysis.

2. Sample

The GMRF structure studied here was fabricated using a nanoreplica molding process described in detail by Yang *et al.* (Fig. 1) [10]. UV-cured polymer (UVCP) atop a polyethylene terephthalate (PET) substrate received the pattern from a silicon master with a 2D square lattice of 150-nm diameter circular posts on a 300-nm period. After UV curing, a thin film of titanium dioxide (TiO₂) with high refractive index ($n = 2.42$ at $\lambda = 532$ nm) is sputter deposited on top of the UVCP to serve as a high refractive index layer over the low refractive index ($n_{UVCP} = 1.45$ at $\lambda = 532$ nm) replica-molded grating structure to produce a PC structure that results in resonant optical reflection. A successive nanoreplica molded UVCP layer may then be fabricated atop the TiO₂ layer, and the process continued. The structure studied here is a stack of three PC filters. The thicknesses of the UVCP layers that are sandwiched between the TiO₂ films are ~ 5 μm , which is substantially greater than the designed resonant wavelength. As a result, there is no mode coupling between the PC layers, each layer behaves as an independent filter, and there is no requirement for tight tolerance on either the thickness of the UVCP layer or the lateral alignment of upper PC filters with respect to filters beneath.

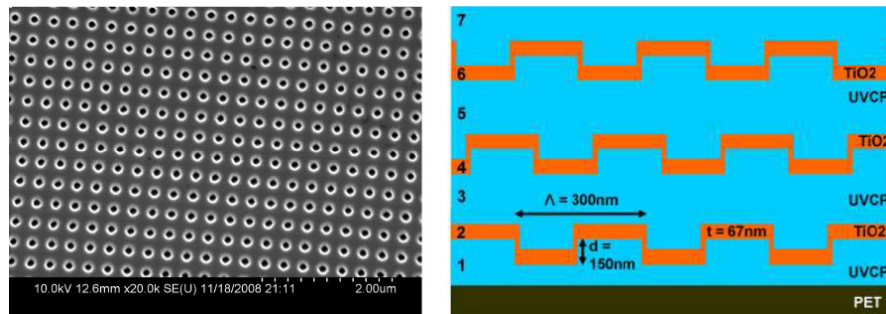


Fig. 1. (left) SEM view of the nanoreplica mold from a 2-D square lattice PC silicon master. The master is comprised of posts resulting in a nanoreplica mold of 2D square lattice of holes. (right) Cross section schematic view of a 3-PC stack filter with 300-nm period, hole depth of 150 nm, and TiO₂ thickness of 67 nm. The schematic cross section is not to scale, as the UVCP layers (layers 1, 3, and 5) are each ~ 5 μm thick, and the PET substrate is ~ 250 μm thick [10].

3. Spectral transmission measurements

Spectral transmission of this three-layer GMRF was measured for off-normal incidence and p-, s- and un-polarized incident light using a Cary 500 Spectrophotometer, a grating monochromator with a Littrow mount. The angular resolution of these measurements was typically 5°; however, for the un-polarized measurements, 1° steps were taken between 24° < θ_i < 27°. ($\theta_i \approx 25^\circ$ will prove of interest later.) These measurements are shown in Figs. 2(a)-2(d).

Analysis of the spectral transmission measurements was performed by developing spectral transmission and reflection simulations for one layer of this GMRF structure in a 3-D finite-difference time-domain (FDTD) Maxwell's equation solver as functions of incident angle and polarization. Specifically, Lumerical FDTD® was used. The structure's geometry in simulation was built using circular features following the circular posts described for the

nanoreplica mold silicon master [10]. Figure 3 shows a schematic of the simulated structure. Definitions for all refractive indices also followed Yang [10]. The unit cell of the simulation consisted of one period ($\Lambda = 300$ nm) in the x- and y-directions using Bloch boundary conditions, and a 600-nm span in the z-direction (transverse to the PC layer) with a Perfectly Matched Layer (PML) boundary condition.

Using this configuration, the plane wave excitation begins inside the UVCP (ϵ_1 in Fig. 3) and the wavelength was adjusted accordingly. Also, to compare the simulated data directly to measured data, the incident angle was adjusted by Snell's law,

$$\theta_{i-sim} = \sin^{-1} \left(\frac{1}{n_{UVCP}} \sin \theta_{i-meas} \right) \quad (2)$$

where θ_{i-sim} is the incident angle in the simulation, n_{UVCP} is the refractive index of UVCP, and θ_{i-meas} is the incident angle in the measurements and the incident angle at which all simulation data is presented.

Simulated sweeps in incident angle, θ_i , wavelength, λ , for s-, p- and un-polarized light, and for azimuthal orientation of the 2-D GMRF structure with respect to the plane of incidence ($\phi = 0$ or 45°) were completed. The hemispherical transmission and reflection were measured with two Frequency Domain Power Monitor (FDPM) planes with their normals in the z-direction. The transmission monitor was placed below the structure and the reflection monitor above the source. Results are shown in Fig. 4.

The measured data of Figs. 2(a)-2(d) and the simulated data of Fig. 4 can also be analyzed by considering it to be the simple phase-matching problem of a grating-coupled waveguide.

$$k \sin(\theta_i) \pm m \frac{2\pi}{\Lambda} = \beta_m = k n_{eff} \quad (3)$$

where k is the propagation constant, Λ is grating period, and β_m is the waveguide propagation constant of the m^{th} mode, where n_{eff} is the effective refractive index in which the m^{th} mode propagates. Since GMRF's are designed for resonance at $\theta_i = 0$ for the $m = 1$ mode, n_{eff} was approximated here as $n_{eff} = \lambda_{\theta=0, m=1} / \Lambda$. For the 2-D GRMF studied here,

$$\vec{k}_x + \vec{k}_y \pm i\vec{G}_y \pm j\vec{G}_x = \vec{\beta}_{i,j} \quad (4)$$

where $\vec{k}_x = k \sin \theta_i \cos \phi \hat{x}$, $\vec{k}_y = k \sin \theta_i \sin \phi \hat{y}$, \hat{x} and \hat{y} are unit vectors in the $\phi = 0$ and 90° directions, respectively, i and j are integers, $|\vec{G}_x| = |\vec{G}_y| = 2\pi / \Lambda$ and $|\beta_{i,j}|$ is again the propagation constant of the i^{th} , j^{th} mode. Equation (3) can be rewritten as,

$$\lambda_{i,j}(\theta_i, \phi) = \frac{\lambda_{\theta=0; i,j=1}}{\sqrt{\left(\frac{\Lambda}{\lambda_{i,j}} \sin \theta_i \sin \phi \pm i \right)^2 + \left(\frac{\Lambda}{\lambda_{i,j}} \sin \theta_i \cos \phi \pm j \right)^2}} \quad (5)$$

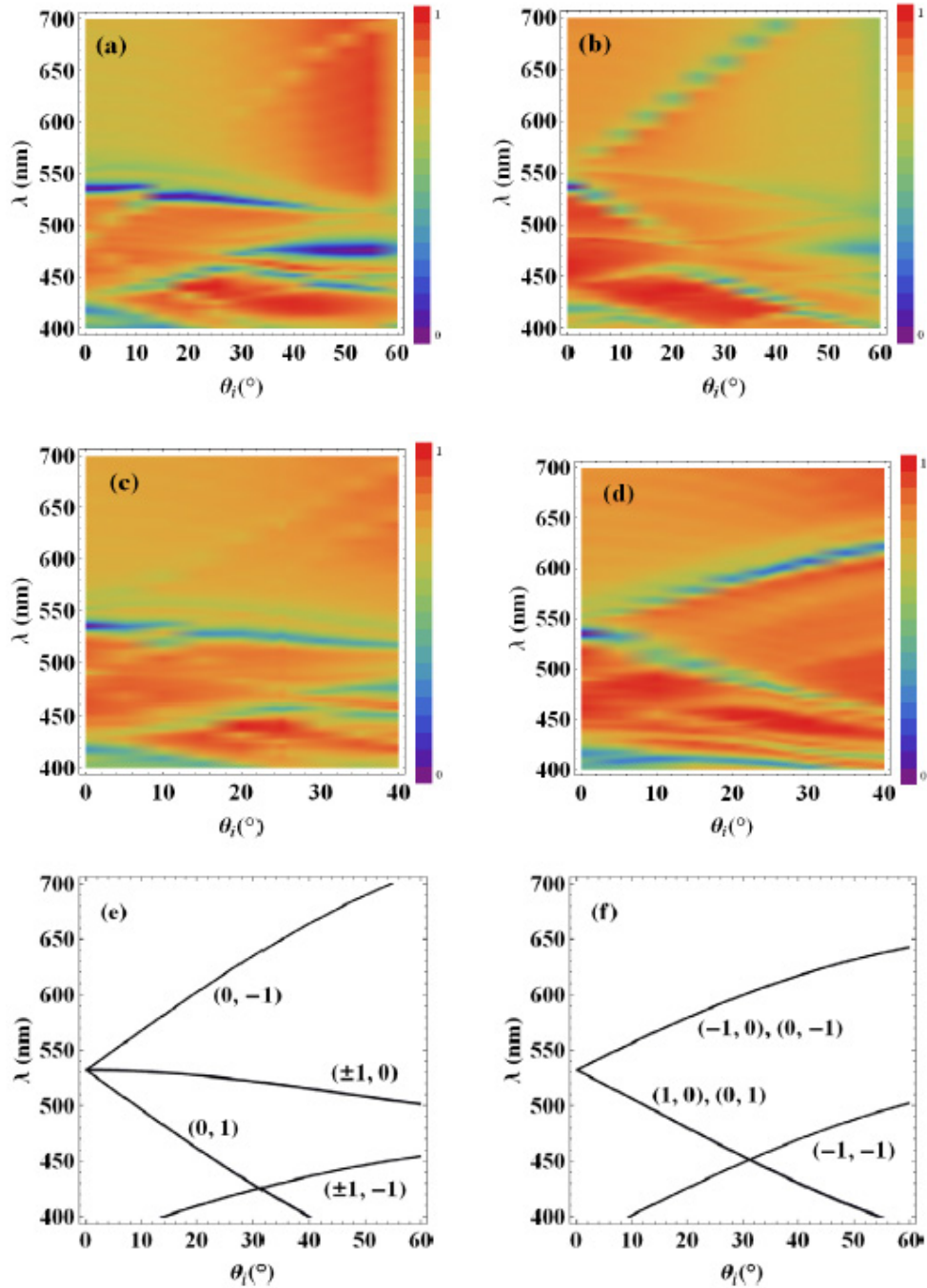


Fig. 2. Measured transmittance of the 2-D GMRF for plane of incidence parallel to the grating periodicity ($\phi = 0$) for (a) p-, (b) s- and (c) un-polarized light, and (d) plane of incidence at 45° from the grating periodicity ($\phi = 45^\circ$). θ_i steps were made in 5° increments, except in (c) and (d) near the angle of interest, 25° , where 1° steps were made. (e) and (f) Solutions to grating-coupled waveguide analysis of Eq. (5) scaled by Snell's law as described in Eq. (2) for (e) $\phi = 0$ and (f) $\phi = 45^\circ$. Here, $n_{\text{eff}} = \lambda_{\phi = 0, m = 1} / \Lambda = 532\text{nm} / 300\text{nm}$, the design wavelength and periodicity of the measured GRMF.

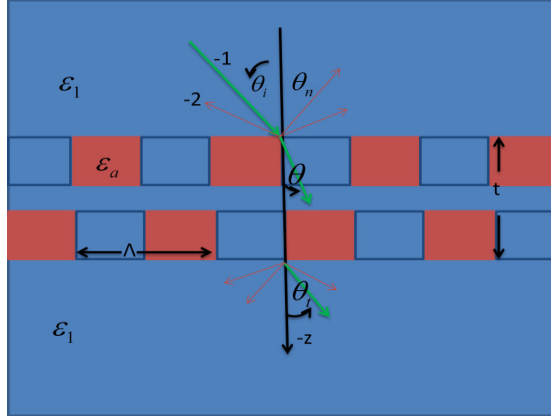


Fig. 3. Cross section schematic view of the simulated GMRF structure. The unit cell consists one period ($\Lambda = 300$ nm) in the x- and y-directions and a 600-nm span in the z-direction. $t = 0.25$ μm . $\epsilon_1 = 2.13$ and $\epsilon_a = 5.86$.

which is plotted in Figs. 2(e) and 2(f) for $\phi = 0$ and 45° for $\lambda_{\theta=0;i,j=1} = 532$ nm and $\Lambda = 300$ nm. Once again, θ_i scaled by Snell's law as described in Eq. (2). Note that this grating-coupled waveguide analysis compares very well with both the measurements of Figs. 2(c) and 2(d) and the simulations of Figs. 4(e) and 4(f).

4. BSDF measurements

The BSDF measurements presented here were made with a Schmitt Measurement Systems, Inc. Complete Angle Scatter Instrument (CASI) using a 544-nm wavelength HeNe laser. The CASI detector is located on a goniometric arm 50 cm away from the sample behind one of four 300- μm to 1.385-cm diameter apertures, implying the solid angle in which the scatter distribution ranged 71 nSr-151 μSr . The detector field of view includes the laser spot on the sample and little significant area outside this, and has a chromatic filter for 544 nm. The CASI also uses a chopper and lock-in detection, making measurements relatively insensitive to ambient light. Calibration experiments against a National Institute of Standards and Technology (NIST) certified reflectance standard showed that the BSDF values are within 2% of the expected value when the system is aligned for the 544-nm source [28].

The CASI is designed for in-plane measurements; *i.e.* the collection receiver stays in the plane created by the incident beam and the surface normal of a vertically oriented sample for both reflection and transmission. In this fashion, the polarization angle of incident and scattered light relative to the sample is insensitive to rotation of the sample about a vertical axis on the surface of the sample. The incident laser polarization is neither perfectly linear nor perfectly aligned either vertically or horizontally. Therefore, a polarizer and half-wave plate were used to ensure the largest incident power and rotate an incident linear polarization state into vertical or horizontal alignment. The polarization state of the scattered light was not collected.

Measurements out of the plane of incidence are accomplished by rotating the sample about a horizontal axis on its surface. The CASI system is basically designed for in-plane measurements; however, by rotating the sample about its horizontal axis, it is possible to collect out-of-plane BSDF data. The θ_i and θ_s values produced by the CASI from a tilted sample assume the sample is vertical. Therefore, a geometric coordinate transformation was applied to the BSDF measurements to ensure the results are presented in the sample-centered coordinate system. The transform used here was described in detail by Germer [29].

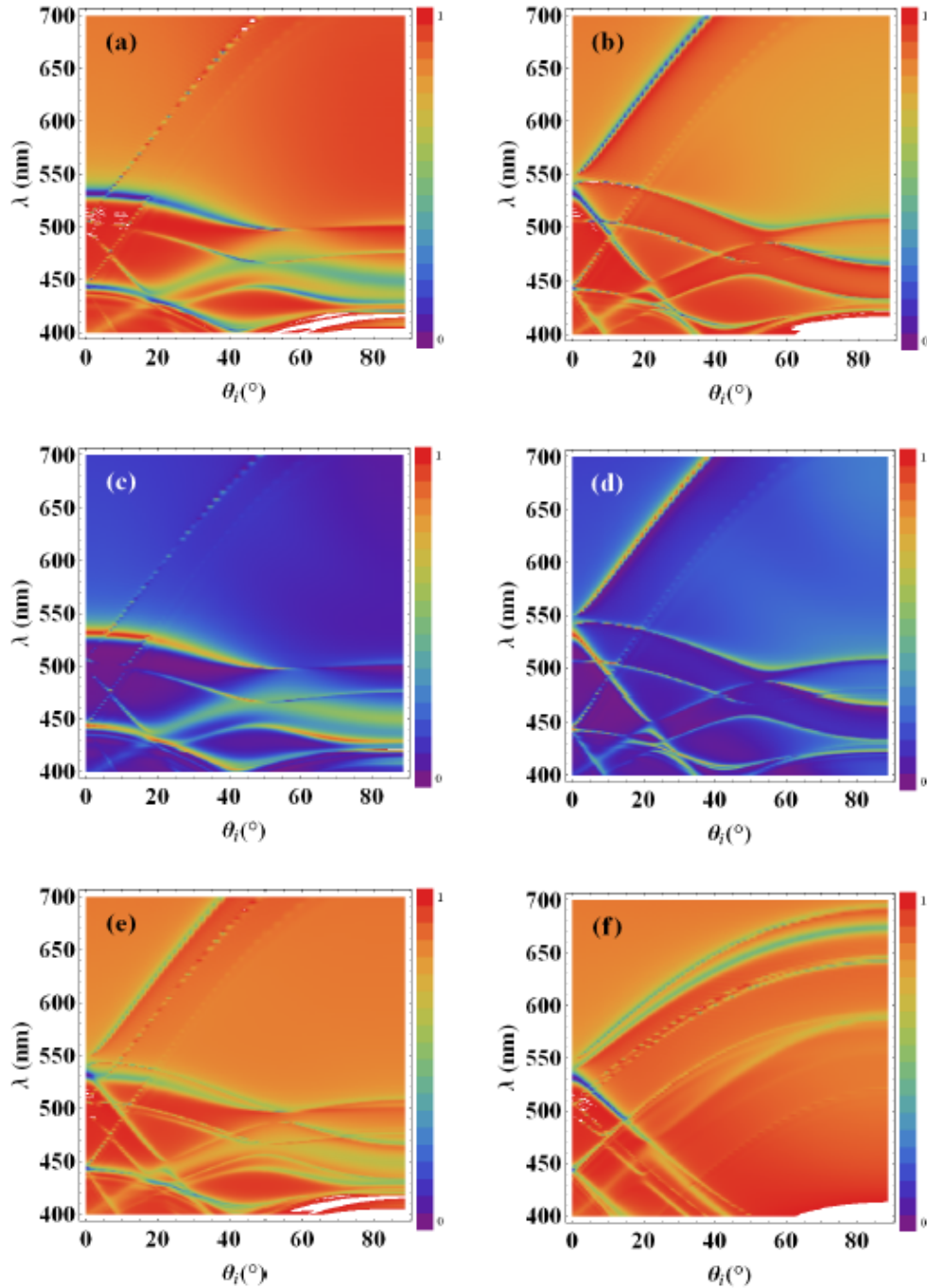


Fig. 4. Simulated transmittance and reflectance of the 2-D GRMF structure as a function of incident angle and wavelength for $\phi = 0$. (a) and (b) Transmittance for p- and s-polarizations. (c) and (d) Reflectance for p- and s-polarizations. (e) and (f) Transmittance for un-polarized light for $\phi = 0$ and $\phi = 45^\circ$.

The BSDF of this PC structure, designed to be a GMRF for normally incident light at 532 nm, was measured at 544 nm. In-plane results for transmittance and reflectance distributions for $\phi = 0$ are shown in Fig. 5. The ridges at $\theta_i = \theta_{tr}$ show the collinear transmittance/specular

reflectance. The curved ridges at the lower right of the BRDF plots ((c) and (d)) correspond to the $m = -1$ diffraction grating order,

$$\sin \theta_m = \frac{m \lambda}{\Lambda} + \sin \theta_i \quad (6)$$

Note the increased retro-reflection in the BRDF at $\theta_i \approx 25^\circ$ and the corresponding increased transmittance at that incident angle in BTDF ((a) and (b)), and the lower-magnitude ridges apparent at $\theta_i \approx 25^\circ$ and $\theta_{t,r} \approx 25^\circ$ in all plots.

The data for in-plane s-polarized BTDF and BRDF at $\theta_i = 25.7^\circ$ is shown in Figs. 6(a) and 6(b). Here, it is obvious that the increased scatter is due to out-coupled diffraction orders. Out-of-plane BRDF measurements were also made at $\theta_i = 15^\circ$ and 35° . Although some out-coupled diffraction was also observed at these angles, its magnitude was much less than that at 25.7° . Note the missing BRDF data in Fig. 6(a) at $\sim 21^\circ < \theta_s < \sim 29^\circ$ is due to the detector occluding the incident laser. Figure 6(c) is a photograph of the reflected diffraction pattern over a $\sim 5^\circ$ solid angle centered on the specular direction at $\theta_i = 25.7^\circ$. Out-of-plane BRDF measurements for both p- and s-polarizations are shown in Figs. 6(d) and 6(e). The appearance of this data is due to the nature of the out-of-plane measurements being made as individual slices across the reflectance hemisphere. For this reason, it was difficult to capture all the out-of-plane diffraction orders, making this an incomplete measurement set.

To analyze the BSDF measured at $\lambda = 544$ nm and $\theta_i = 25.7^\circ$ further, a second Lumerical FDTD® simulation was performed, modeling the GMRF structure as a single-layer 2-D PC sandwiched by 500 nm of UVCP on the top and bottom. Grating orders and their strengths were calculated in all directions. In the z-direction (again, transverse to the PC layer), only specular grating orders were calculated. However, in the x- and y-directions, multiple grating orders were calculated and their strengths determine power propagating parallel to the grating periodicity. These results are shown in Fig. 7, where normalized x/y transmission corresponding to the wavelength and incident angle points shown in the inset is plotted. The inset shows s-polarization transmittance as a function of λ and θ_i , similar to Fig. 4(b). Since the GMRF was designed for destructive interference of the design wavelength (532 nm) upon transmission at normal incidence, normalized x/y transmission of the $m = 1$ modes at $\theta_i = 0$ is zero, as expected. The x/y transmission of all the modes then increases with incident angle.

Grating orders and their directions for three of the λ and θ_i locations shown in the inset of Fig. 7, A, B and C, are shown in Fig. 8. The black dotted lines represent the incident light, the blue lines represent the specular reflection, and the red and green lines represent the magnitude of the power transmitted in the x- and y-directions. (A) For normal incidence at 532 nm, essentially no power is transmitted into the structure. (B) For off-normal incidence at wavelengths not corresponding to a grating-coupled mode, x/y transmission is also minimal. But (C), for off-normal incidence at wavelengths corresponding to coupled modes, x/y transmission is significant, and leads to the out-coupling seen in our BSDF measurements.

5. Conclusion

This work investigated the BSDF at incident angles other than normal and at 544-nm wavelength of a GMRF PC structure designed for normally incident light at 532 nm. We found strongly out-coupled PC diffraction orders into both the transmittance and reflectance hemispheres for light incident at 25.7° . Our analysis included developing a full 3-D FDTD Maxwell's equation solution to this experiment, and we found such out-coupled diffraction should be expected whenever the incident angle and wavelength match one of the grating modes for the PC structure. The 544-nm wavelength/ 25.7° incidence angle combination here

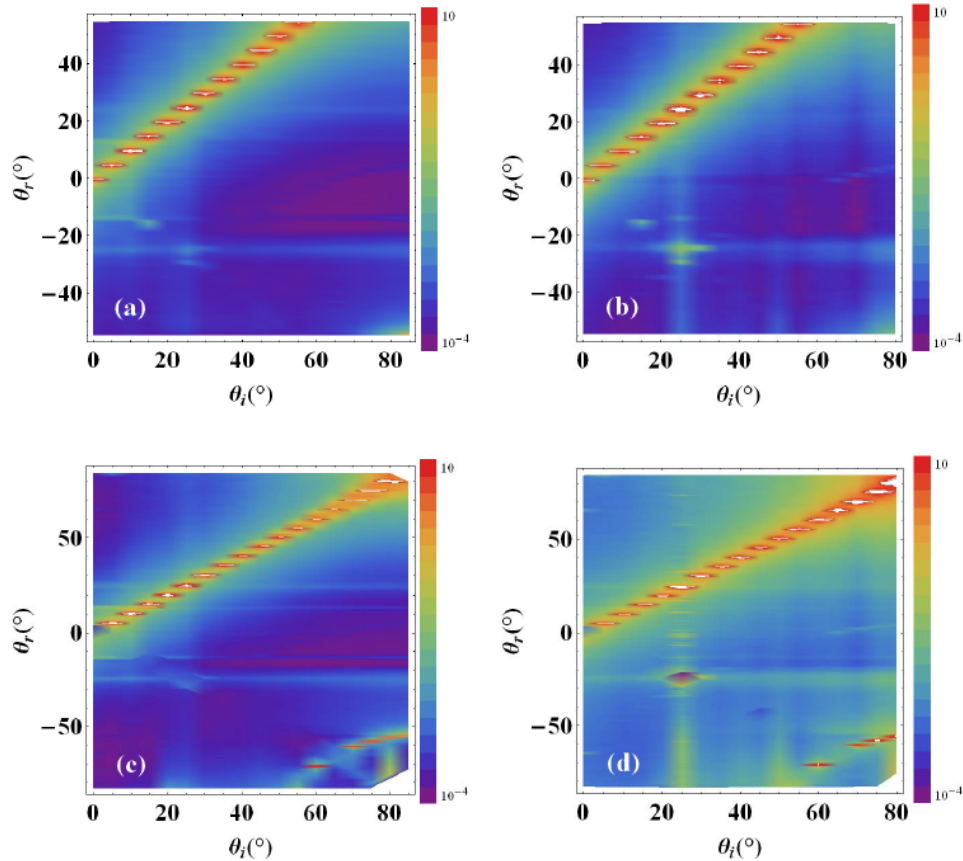


Fig. 5. In-plane Log(BTDF) of GMRF structure measured at $\lambda = 544$ nm for (a) p- and (b) s-polarizations, and in-plane Log(BRDF) measurements for (c) p- and (d) s-polarizations. Note that the collinear transmittance/specular reflectance peaks at $\theta_i = \theta_{i,r}$ have magnitudes greater than 10 Sr^{-1} as do the $m = -1$ diffraction order peaks in (c) and (d).

appears to match well with the $(\pm 1, 0)$ PC grating mode. Our simulations also show that since this GMRF was designed for complete destructive interference of the transmitted light upon normal incidence, stronger out-coupled diffraction should be expected for modal solutions as the angle of incidence increases. BSDF measurements at incident angles of 15° and 35° also displayed out-coupled diffraction, though much lower in magnitude, which is again attributed to these incidence angle/wavelength pairs being weaker matches to the $(\pm 1, 0)$ mode.

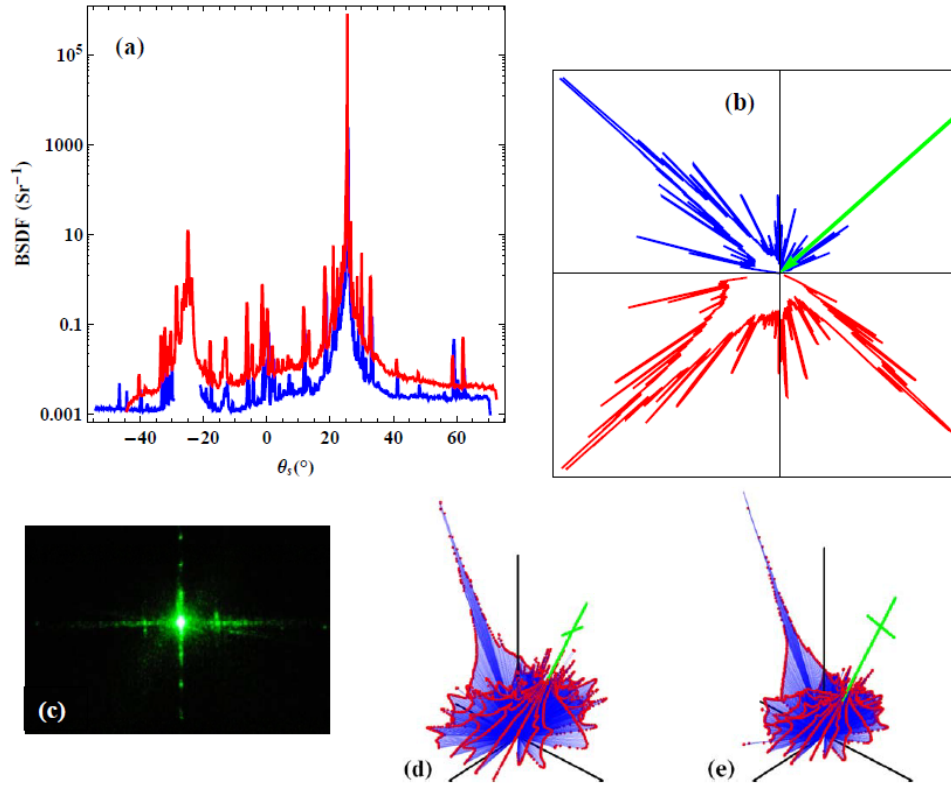


Fig. 6. (a) and (b) In-plane Log(BSDF) of the GMRF (design wavelength of 532 nm) measured at 544 nm at $\theta_i = 25.7^\circ$. BTDF is shown in red and BRDF in blue. (a) Log-linear plot: The BRDF occlusion region around $\theta_r = -25.7^\circ$ is due to the detector blocking the incident beam. (b) Log-polar plot: The green arrow shows the incident angle of 25.7° . (c) Photo of both in-plane and out-of-plane reflected scatter centered about the specular direction at $\theta_i = 25.7^\circ$. (d) and (e) Out-of-plane Log(BRDF) at $\theta_i = 25.7^\circ$ for (d) p- and (e) s-polarizations.

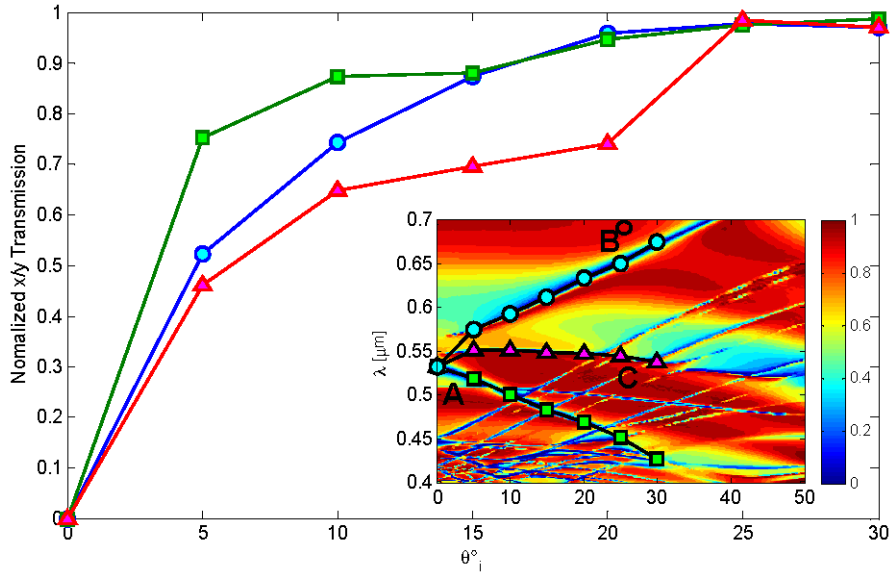


Fig. 7. Normalized x/y transmission for seven points along the $(0, -1)$, $(\pm 1, 0)$ and $(0, 1)$ modes corresponding to the λ and θ_i points shown in the inset. The inset shows the transmittance of s-polarized radiation as a function of wavelength and incident angle. The A, B, and C points on the inset correspond to the λ and θ_i values at which the grating orders are plotted in Fig. 8.

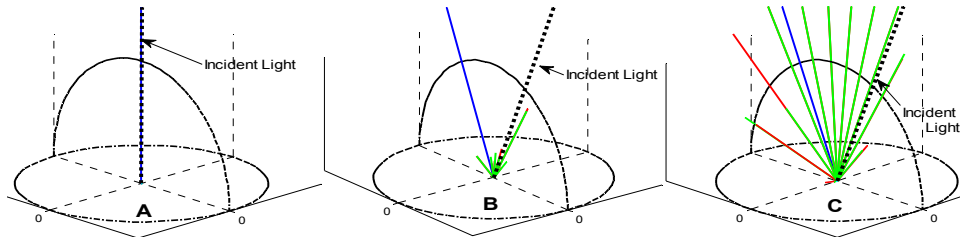


Fig. 8. Spherical plots of grating orders and their directions. (A) $\lambda = 532$ nm and $\theta_i = 0^\circ$, (B) $\lambda = 700$ nm and $\theta_i = 25^\circ$, and (C) $\lambda = 544$ nm and $\theta_i = 25^\circ$. The black dotted lines represent the incident light, the blue lines represent the specular reflection, and the red and green lines represent the light transmitted in the x- and y-directions.

Acknowledgments

The research was supported by the Air Force Research Laboratory, Wright-Patterson AFB OH. The views expressed in this paper are those of the authors and do not necessarily reflect the official policy or position of the Air Force, the Department of Defense or the U.S. Government.